


Demonstration of sub-GV/m accelerating field in a photoemission electron gun powered by nanosecond X-band radio-frequency pulses

W. H. Tan¹, S. Antipov², D. S. Doran³, G. Ha³, C. Jing^{2,3,*}, E. Knight², S. Kuzikov^{2,†},
W. Liu³, X. Lu^{1,3}, P. Piot^{1,3,‡}, J. G. Power³, J. Shao³, C. Whiteford³, and E. E. Wisniewski³

¹Northern Illinois Center for Accelerator & Detector Development and Department of Physics,
Northern Illinois University, DeKalb, Illinois 60115, USA

²Euclid Techlabs LLC, Bolingbrook, Illinois 60440, USA

³Argonne National Laboratory, Lemont, Illinois 60439, USA

 (Received 23 March 2022; revised 3 June 2022; accepted 11 August 2022; published 24 August 2022)

Radio-frequency (rf) photoemission electron guns operating at higher accelerating gradients offer a pathway to produce brighter electron bunches. Brighter beams are expected to revolutionize many areas of science: they could form the backbone of next-generation compact x-ray free-electron lasers or provide coherent ultrafast quantum electron probes. We report on the experimental demonstration of an rf photoemission electron source supporting an accelerating field close to 400 MV/m at the photocathode surface without major rf breakdown or significant dark current over a 3-week experimental run. This unprecedented gradient was achieved by operating the gun in a new regime with short rf pulses, ~ 9 ns X-band (11.7 GHz). The demonstrated paradigm provides a viable path to form relativistic electron beams with unprecedented brightness.

DOI: [10.1103/PhysRevAccelBeams.25.083402](https://doi.org/10.1103/PhysRevAccelBeams.25.083402)

Charged-particle accelerators have been invaluable engines of discovery in fundamental sciences since their inception in the early 20th century. Bright electron beams have enabled the development of accelerator-based light sources, i.e., free-electron lasers (FELs), capable of producing coherent radiation over a broad range of the electromagnetic spectrum [1]. Additionally, directly employing bright electron beams as primary probes, e.g., in ultrafast electron scattering, has produced groundbreaking research in condensed-matter physics and chemistry [2]. A critical aspect to the generation of bright electron beams is the rapid acceleration of the bunch during the emission process to mitigate space-charge effects. Specifically, the beam peak brightness $\mathcal{B} = q/\Gamma$, where q is the bunch charge and Γ its six-dimensional phase-space volume, scales with the electric field E_a experienced during emission at the emitter surface as $\mathcal{B} \propto E_a^\alpha$ where the exponent $\alpha \geq 1$ depends on the bunch's initial transverse-to-longitudinal aspect ratio [3,4].

Normal-conducting radio-frequency (rf) photoemission electron sources [5,6] (“rf guns”) invented in the mid 80s

support high electric fields that ultimately boosted the development of x-ray FELs [7]. The highest field an rf resonator can sustain is ultimately limited by the peak surface field E_0 on its walls. The performances of high-gradient electron sources ($E_0 > 200$ MV/m) designed in recent years [8–10] have been hindered by rf breakdown—a phenomenon where the material is ejected from the surface of the resonator thus momentarily preventing the storage of electromagnetic energy in the cavity [11]. Besides, these sources often exhibit substantial *dark-current* emissions due to the spurious uncontrolled emission of electrons via quantum tunneling from the surfaces exposed to the high electric fields [12]. In this paper, we demonstrate that the use of short-pulse electromagnetic fields offers a viable path toward the generation of GV/m surface fields in metallic accelerating structures. We specifically confirm the attainment of > 0.5 GV/m electric field on the copper surface of a resonant cavity operating at 11.7 GHz and powered by 9-ns rf pulses. The surface field is calculated by measuring the energy of the electron bunches photoemitted by impinging an ultraviolet laser pulse on the surface. The required high-peak-power short rf pulses are produced via deceleration of a train of relativistic electron bunches (~ 60 MeV) in a slow-wave structure.

Over the past two decades, experimental investigations have shown that the rf-breakdown process in structures operating at room temperature is predominantly correlated with the surface electric field and the rf-pulse width [13–16]. A phenomenological model based on experiments conducted with rf-pulse duration $\tau_p \sim [100, 1000]$ ns

*c.jing@euclidtechlabs.com

†s.kuzikov@euclidtechlabs.com

‡ppiot@niu.edu

suggests that the breakdown rate (BDR) follows the power law $BDR \propto E_0^{30} \tau_p^{-5}$, [15,17,18]. The latter equation implies that for a given BDR, an increase in the field amplitude E_0 can be accommodated by shortening the rf-pulse duration. Despite this well-known scaling law, this approach has not been extended to the sub-100 ns region and is the basis of the present work. Another benefit of the short rf pulses is the mitigation of the average dark current, i.e., the total charge emitted from the structure via mechanisms other than photoemission (i.e., field emission). In our case, the acceleration field only lasts for 9 ns so the average dark current is orders of magnitude smaller than in conventional guns powered by μs rf pulses.

To investigate the generation of short-pulse high electric fields using high peak-power short rf pulses, an X-band rf (XRF) photoemission gun was designed [19]. The gun consists of a $1 + \frac{1}{2}$ -cell resonator functioning on the $\text{TM}_{010,\pi}$ mode at 11.7 GHz; see Fig. 1(a). It is a strongly overcoupled resonator resulting in a low loaded quality factor ($Q_\ell \simeq 180$), thus rapidly establishing the rf field inside the cavity. The gun is made of oxygen-free copper using conventional fabrication techniques combining high-precision machining and hydrogen-furnace brazing. A broadband coaxial rf-input coupler is used to ensure the field distribution remains axisymmetric and ultimately maximize the beam brightness.

The iris disk located between the two cells incorporates four magnetic coupling slots that increase both the rf coupling between cells and the frequency separation from the neighboring resonant $\text{TM}_{010,0}$ mode. Figure 1(b) compares the simulated peak field on the photocathode for the XRF gun being driven by long ($\tau_p = 100$ ns) and short ($\tau_p = 3$ ns) rf pulses and reveals that the maximum field amplitude attained in the transient regime is 67% of the steady-state field (i.e., reached after time $t \simeq 30$ ns). The advantage of operating the gun in the short-pulse mode, as opposed to the long-pulse mode, is that the photocathode experiences the field for 1/10th the time. This, in turn, leads to the ability to operate the gun at a higher gradient with a simultaneously lower dark current.

The XRF gun was integrated into the Argonne Wakefield Accelerator (AWA) [20]. The AWA includes an L-band ($f_L = 1.3$ GHz) rf photoinjector that produces an electron beam arranged as a train of eight high-charge electron bunches separated by $T_L = 1/f_L \simeq 769$ ps. The bunch train (with total charge $Q_{db} \leq 400$ nC) is further accelerated in a linear accelerator to a final energy of ~ 60 MeV before being transversely focused in a power-extraction and transfer structure (PETS) to excite high peak-power rf pulse at $f = 9f_L = 11.7$ GHz [21]. For the experiment reported below, the rf-pulse power was ~ 250 MW (and occasionally up to 300 MW) with a typical rf pulse shape displayed in Fig. 1(b), inset. The rf pulses were outcoupled from the PETS and guided to the XRF gun collocated to the AWA accelerator; see Fig. 1(c). Owing to the 2-Hz repetition rate of the AWA facility, only a few Watts of average rf power is dissipated in the XRF gun despite operating in such a high peak-power regime, thus no water cooling is required.

The XRF gun is nested in a magnetic solenoidal lens that provides control over the beam transverse size and eventually maximizes the beam brightness [22,23]. The downstream beamline includes remotely insertable Ce:YAG scintillating screens to measure the transverse beam distribution and one integrated current monitor (ICT) for bunch-charge measurement. One of the screens (X4) is located at a high-dispersion point downstream of a dipole magnet for energy measurement. The bunches are generated by impinging an ultraviolet (UV) laser pulse (≤ 200 μJ) split off from the ~ 4 -mJ laser pulse producing the high-charge drive bunches. The low-intensity pulse is sent to the experimental area (from mirror M1) after propagating in a ~ 30 -m optical line with imaging lenses and a coarse delay that ensures the laser pulse impinges the photocathode within ~ 2 ns of the rf-pulse injection in the XRF gun. In the experimental area, the laser path comprises a fine adjustable optical delay line (M3-M4) with a range of ± 2 ns, along with a set of lenses (L1, L2) to focus the beam on the photocathode. The laser enters the evacuated XRF-gun beamline where an in-vacuum mirror (M6) directs the pulse on the backplane of the XRF gun which serves as a copper photocathode; see Fig. 1(a). The UV laser on the

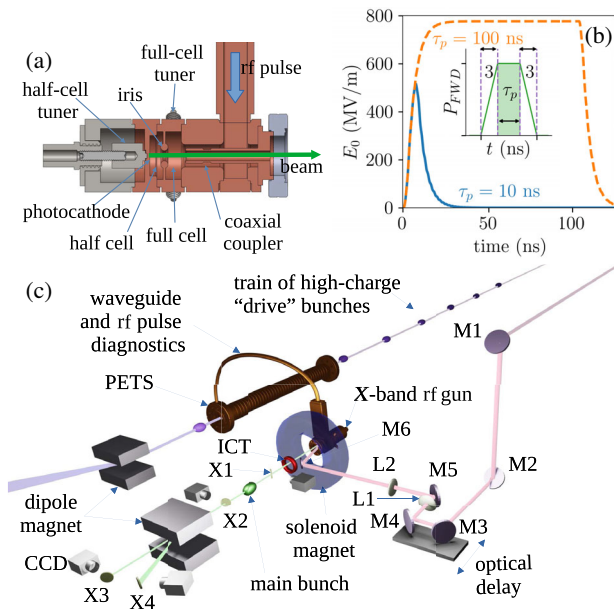


FIG. 1. Schematic of the XRF gun (a) and simulated peak field on photocathode (b) for a short ($\tau_p = 3$ -ns, solid trace) and long ($\tau_p = 100$ -ns, dash trace) flattop 300-MW peak power rf pulse (the inset details the forward power P_{FWD} rf-pulse profile with 3-ns rising and falling edges). Overview of the experimental setup (c): the upper (magenta) path corresponds to the relevant section of the AWA main accelerator and the lower (green) path is the XRF gun beamline. The pink path shows the UV laser path. The labels X_i , M_i , and L_i , respectively, refer to Ce:YAG scintillating screens with CCD cameras, optical mirrors, and lenses.

photocathode has a uniform distribution with a radius of $400\ \mu\text{m}$ with a ~ 400 -fs duration.

The XRF gun was conditioned to photocathode fields $E_0 \simeq 350\ \text{MV/m}$ deduced from the measured forward rf power. Figure 2(a) shows the rf-conditioning history with the evolution of the field amplitude as a function of the number of rf pulses. The latter figure also reports the ratio of the measured over simulated peak values of the reflected power signal. A value of $R = 1$ implies there are no rf breakdowns (or dark current-induced beam loading). Due to the nonideal charge balance of the drive bunch train, the forward-power flattop duration was $\tau_p < 3\ \text{ns}$. In the simulation, we used the measured charge balance combined with the frequency-domain bench measurements of the XRF gun to calculate the input and reflected rf pulse shapes. From Fig. 2(a), we observe three conditioning regions: First, for values $E_0 \leq 150\ \text{MV/m}$, the field increases monotonically with $R \simeq 1$. Then, at $E_0 \simeq 150\ \text{MV/m}$, the ratio $R \leq 1$ and decreases until it reaches its minimum for fields $E_0 \simeq 250\ \text{MV/m}$ due to breakdown event and dark-current emission. Eventually, the XRF gun is conditioned and a value $R \simeq 1$ is recovered for $E_0 \simeq 350\ \text{MV/m}$ (after 5×10^4 rf pulses, with forward power $P_{\text{FWD}} \simeq 250\ \text{MW}$ corresponding to $Q_{\text{db}} \simeq 350\ \text{nC}$). At the time of the conditioning, the maximum field amplitude attained was capped by the available rf power. The entire conditioning process took only 7×10^4 pulses (i.e., $\sim 10\ \text{h}$ at 2-Hz repetition rate). Ultimately, the field was set to $E_0 \simeq 200\ \text{MV/m}$, to confirm the absence of any additional breakdown events or dark-current emissions. Subsequently,

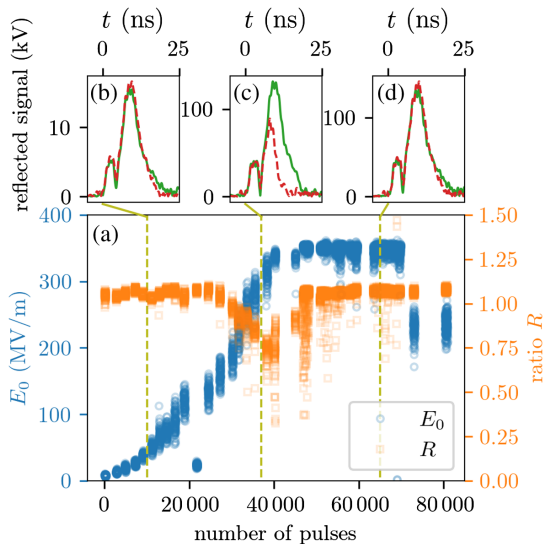


FIG. 2. rf conditioning history of the XRF gun (a) where the photocathode peak field E_0 was gradually increased (blue circle) and the ratio of the peak value of the measured to simulated reflected rf signals, R , recorded (orange square). The upper plots (b)–(d) compared the measured (dash red trace) and simulated (green solid trace) rectified rf-reflection signals at different stages of the conditioning history indicated with the dash vertical lines.

the XRF gun was operated up to $\sim 400\ \text{MV/m}$ during the photoemission experiment and no dark current could be detected on the ICT or Faraday cup. We resorted to use the pixels noise level associated with the data recorded at X1 while scanning the solenoid magnetic field to estimate an upper bound value of $\sim 1\ \text{pC}$ for the dark-current charge emitted over the entire rf pulse. This estimate assumes the number of electrons is proportional to the light intensity in each pixel which was *a priori* calibrated against the ICT for the photoemitted beam. Likewise, the accumulated statistics over $\sim 500,000$ shots gives a conservative upper limit for the BDR of 10^{-5} .

After conditioning, the UV laser pulse was injected into the XRF gun. Coarse and fine timing scans were performed to find the optimal injection time of the laser pulse into the rf pulse. The coarse scans were performed by adjusting the optical delay of the incoming laser to vary its launch phase φ_0 over several rf cycles. During these “phase scans,” the field experienced during emission varies as $E_a = E_0 \sin \varphi_0$ and the photoemitted charge is recorded leading to the localization of several rf buckets. Subsequently, fine scans were performed over the emission period $\varphi_0 \in [0, 360]^\circ$ as shown in Fig. 3(a) and confirmed the photoemission of bunches with charges up to $q = 60 \pm 25\ \text{pC}$. The evolution of the emitted charge is also characteristic of Schottky-assisted photoemission resulting from the lowering of the potential barrier in presence of applied high electric fields at the photocathode surface [24]. The ASTRA beam-dynamics program [25] was employed to simulate the phase scan. The simulation without accounting for the Schottky effect shows the phase scan follows a plateau-shaped distribution with a slight dip for $\varphi_0 \in [50, 100]$ attributed to particle loss on the iris aperture. However, including the Schottky effect using a model where the charge of the N macroparticles representing the bunch in ASTRA scales as $q_m = q/N + \xi \sqrt{E_0 \sin \varphi_m}$, where $\varphi_m \equiv \varphi_0 + 2\pi f t$ is

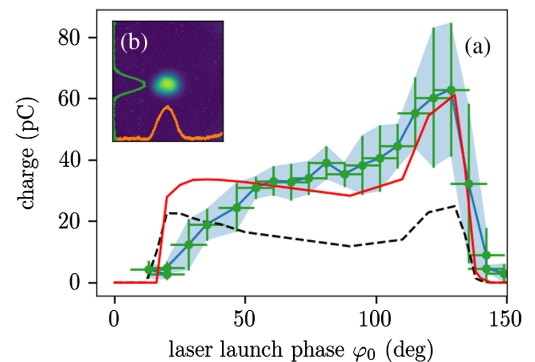


FIG. 3. Measured bunch charge as a function of laser-launch phase (circles with shaded area giving the uncertainty) compared with ASTRA simulations with (solid line, Schottky-strength parameter set to $\xi = 2 \times 10^{-3}$) and without (dash line, $\xi = 0$) including the Schottky effect. The inset (b) gives the transverse beam distribution on a $10 \times 10\ \text{mm}^2$ area at X1 for $\varphi_0 \simeq 95^\circ$ with associated projections (solid lines).

emission phase of the m th macroparticle and ξ controls the strength of the Schottky effect, produces a simulated phase-scan distribution with similar features as on the measured scan [see Fig. 3(a)]. The transverse beam density measured at X1 appears in Fig. 3(inset b).

The kinetic energy downstream of the gun was measured using the scintillating screen X4 located downstream of a dipole magnet. The beam is first aligned on the reference orbit using the scintillating screens X2 and X3 and uncertainties on the incoming reference trajectory limit the energy resolution to $\Delta K/K \simeq 1.7 \times 10^{-2}$. The kinetic energy is a bivariate function $K(E_0, \varphi_0)$ obtained by solving a set of coupled ordinary differential equations [26,27]. We used ASTRA to numerically compute the function $K(E_0, \varphi_0)$ over a 28×86 two-dimensional grid for $E_0 \in [315, 450]$ MV/m and $\varphi_0 \in [45^\circ, 130^\circ]$. A spline-interpolated function $K(E_0, \varphi_0)$ was then used to calculate the value of E_0 given the measured kinetic energy and operating phase φ_0 . The contour plot of $K(E_0, \varphi_0)$ and inferred fields values appear in Fig. 4. The area enclosed by two kinetic-energy isoclines and two vertical lines of operating phase, obtained via error propagation of the energy-measurement and launch-phase uncertainties, provide the error region of the calculated field with its upper and lower error bounds. The result of such an analysis confirms that the maximum peak field attained during our experiment was $E_0 = 387.76_{-35.88}^{+44.63}$ MV/m corresponding to a surface field at the iris of $1.55E_0 \simeq 601.03_{-51.61}^{+69.18}$ MV/m. These field strengths were consistently reached over extended periods during the 3-week experimental run.

Figure 5(a) displays a waterfall plot of stacked energy spectra for successive shots acquired over a 15-min period. The data reveal the kinetic energy jitter over the period to be $\frac{\Delta K}{K} \simeq 1.4\%$ (rms) and consist of a shot-to-shot jitter superimposed with a long-term (~ 5 min) drift. The latter slow

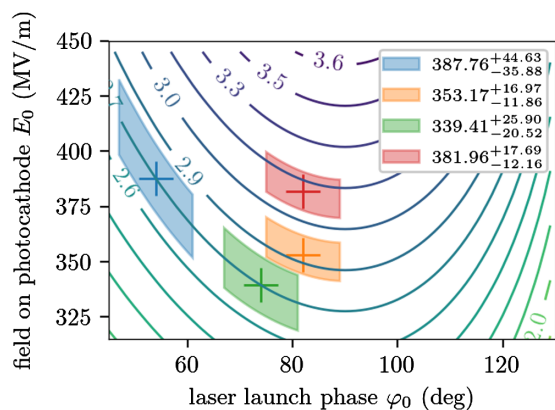


FIG. 4. Simulated kinetic-energy isoclines as a function of rf-gun operating conditions $K(E_0, \varphi_0)$ and retrieved operating points (“+” symbols) for four measurements. The labeled isoclines give the kinetic energy in MeV units. The shaded areas represent the uncertainty on the measured φ_0 and inferred E_0 values (reported in the legend in MV/m units).

oscillation appears to be partially correlated to the drive-beam charge fluctuation [see Figs. 5(a) and 5(b)]. During our experiment, the drive-beam charge relative fluctuation was $\frac{\Delta Q_{db}}{Q_{db}} \simeq 4.9\%$ (rms) and the bunch charge photoemitted from the XRF gun was $q = 86.2 \pm 16.1$ pC; see Figs. 5(e) and 5(f). The XRF-gun charge jitter is dominated by phase and amplitude jitters due to the drive-beam jitter and drift which impacts Q_{db} ; see Fig. 5(d). The overall stability of the XRF gun is limited by the current experimental configuration. Removing long-term drift indicates that the Q_{db} has a shot-to-shot jitter of 4.7% compared to the UV-laser energy jitter on the drive-beam photocathode.

In conclusion, we demonstrated the generation of relativistic (~ 3 MeV) electron bunches from an ultrahigh gradient X-band rf gun powered by nanoseconds rf pulses. The gun supports photocathode fields $E_0 \sim 400$ MV/m—i.e., ~ 3 times larger than reliably attained in previous setups—without any observable breakdown or detectable dark current. Such an accomplishment confirms that powering accelerating structures with short rf pulses provide a viable path to establish GV/m peak electric fields for generating bright ultrarelativistic electron bunches with applications to advanced accelerators and compact light sources.

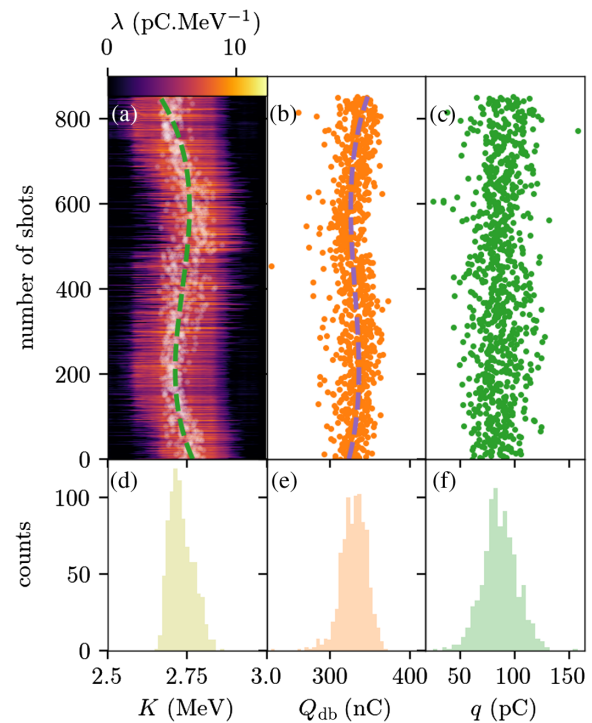


FIG. 5. Waterfall plot of measured energy spectra density λ over 853 shots (a) with associated drive-beam charge transmitted through the PETS (b), and corresponding bunch charge photoemitted from the XRF gun (c). Plots (d)–(f) are the associated histograms. The dashed trace in (a) is a spline interpolation of the slow drift which is superimposed as a dashed curve in (b) after applying an affine transformation.

We thank V. Dolgashev (SLAC National Accelerator Laboratory) for his generous support of X-band rf components. This work was supported by the U.S. DOE, under Awards No. DE-SC0018656 and DE-SC0022010 to Northern Illinois University, DOE SBIR Grant No. DE-SC0018709 to Euclid Techlabs LLC. The research uses resources at Argonne National Laboratory funded by the U.S. DOE under Contract No. DE-AC02-06CH11357.

-
- [1] R. Bonifacio, C. Pellegrini, and L. Narducci, Collective instabilities and high-gain regime in a free electron laser, *Opt. Commun.* **50**, 373 (1984).
- [2] J. R. Dwyer, C. T. Hebeisen, R. Ernstorfer, M. Harb, V. B. Deyirmenjian, R. E. Jordan, and R. Dwayne Miller, Femtosecond electron diffraction: Making the molecular movie, *Philos. Trans. R. Soc. A* **364**, 741 (2006).
- [3] I. V. Bazarov, B. M. Dunham, and C. K. Sinclair, Maximum Achievable Beam Brightness from Photoinjectors, *Phys. Rev. Lett.* **102**, 104801 (2009).
- [4] D. Filippetto, P. Musumeci, M. Zolotarev, and G. Stupakov, Maximum current density and beam brightness achievable by laser-driven electron sources, *Phys. Rev. ST Accel. Beams* **17**, 024201 (2014).
- [5] J. Fraser, R. Sheffield, and E. Gray, A new high-brightness electron injector for free electron lasers driven by rf linacs, *Nucl. Instrum. Methods Phys. Res., Sect. A* **250**, 71 (1986).
- [6] K. McDonald, Design of the laser-driven rf electron gun for the BNL accelerator test facility, *IEEE Trans. Electron Devices* **35**, 2052 (1988).
- [7] B. W. J. McNeil and N. R. Thompson, X-ray free-electron lasers, *Nat. Photonics* **4**, 814 (2010).
- [8] C. Limborg-Deprey, C. Adolphsen, D. McCormick, M. Dunning, K. Jobe, H. Li, T. Raubenheimer, A. Vrieling, T. Vecchione, F. Wang, and S. Weathersby, Performance of a first generation x-band photoelectron rf gun, *Phys. Rev. Accel. Beams* **19**, 053401 (2016).
- [9] R. A. Marsh, G. G. Anderson, S. G. Anderson, D. J. Gibson, C. P. J. Barty, and Y. Hwang, Performance of a second generation X-band rf photoinjector, *Phys. Rev. Accel. Beams* **21**, 073401 (2018).
- [10] M. A. K. Othman, J. Picard, S. Schaub, V. A. Dolgashev, S. M. Lewis, J. Neilson, A. Haase, S. Jawla, B. Spataro, R. J. Temkin, S. Tantawi, and E. A. Nanni, Experimental demonstration of externally driven millimeter-wave particle accelerator structure, *Appl. Phys. Lett.* **117**, 073502 (2020).
- [11] G. N. Fursey, Field emission and vacuum breakdown, *IEEE Trans. Electr. Insul.* **EI-20**, 659 (1985).
- [12] R. H. Fowler and L. Nordheim, Electron emission in intense electric fields, *Proc. R. Soc. A* **119**, 173 (1928).
- [13] V. Dolgashev, S. Tantawi, Y. Higashi, and B. Spataro, Geometric dependence of radio-frequency breakdown in normal conducting accelerating structures, *Appl. Phys. Lett.* **97**, 171501 (2010).
- [14] L. Laurent, S. Tantawi, V. Dolgashev, C. Nantista, Y. Higashi, M. Aicheler, S. Heikkinen, and W. Wuensch, Experimental study of rf pulsed heating, *Phys. Rev. ST Accel. Beams* **14**, 041001 (2011).
- [15] A. Grudiev, S. Calatroni, and W. Wuensch, New local field quantity describing the high gradient limit of accelerating structures, *Phys. Rev. ST Accel. Beams* **12**, 102001 (2009).
- [16] J. Shao, H. Chen, D. Doran, G. Ha, C. Jing, X. Lin, W. Liu, M. Peng, J. Power, J. Shi, C. Whiteford, E. Wisniewski, and H. Zha, Demonstration of gradient above 300 MV/m in short pulse regime using an x-band single-cell structure, in *Proceedings of the 10th International Particle Accelerator Conference, IPAC2022, Bangkok, Thailand* (JACoW, Geneva, Switzerland, 2022), FROXSP2, [10.18429/JACoW-IPAC2022-FROXSP2](https://doi.org/10.18429/JACoW-IPAC2022-FROXSP2)
- [17] S. Döbert, R. Fandos, A. Grudiev, S. Heikkinen, J. A. Rodriguez, M. Taborelli, W. Wuensch, C. Adolphsen, and L. Laurent, High power test of an x-band slotted-iris accelerator structure at NLCTA, *Conf. Proc. C* **070625**, 2191 (2007).
- [18] F. Wang, Breakdown characteristics study on an 18 cell X band structure, *AIP Conf. Proc.* **1086**, 373 (2009).
- [19] S. Kuzikov, S. Antipov, P. Avrakhov, G. Ha, A. Liu, and J. Power, Ultra-high gradient short rf pulse gun, in *Proceedings of the 10th International Particle Accelerator Conference, IPAC-2019, Melbourne, Australia* (JACoW, Geneva, Switzerland, 2019), WEPRB072.
- [20] M. Conde, S. Antipov, D. Doran, W. Gai, Q. Gao, G. Ha, C. Jing, W. Liu, N. Neveu, J. Power, J. Qiu, J. Shao, Y. Wang, C. Whiteford, E. Wisniewski, and L. Zheng, Research Program and Recent Results at the Argonne Wakefield Accelerator Facility (AWA), in *Proceedings of the 8th International Particle Accelerator Conference, IPAC-2017, Copenhagen, Denmark* (JACoW, Geneva, Switzerland, 2017), pp. 2885–2887.
- [21] M. Peng, J. Shao, C. Jing, E. C. Wisniewski, G. Ha, J. Seok, M. Conde, W. Liu, J. G. Power, D. Doran, C. Whiteford, and J. Shi, Generation of high power short rf pulses using an X-band metallic power extractor driven by high charge multi-bunch train, in *Proceedings of the 10th International Particle Accelerator Conference, IPAC-2019, Melbourne, Australia, 2019* (JACoW, Geneva, Switzerland, 2019), MOPRB069.
- [22] L. Serafini and J. B. Rosenzweig, Envelope analysis of intense relativistic quasilaminar beams in rf photoinjectors: mA theory of emittance compensation, *Phys. Rev. E* **55**, 7565 (1997).
- [23] W. H. Tan, G. Chen, G. Ha, C. Jing, S. Kuzikov, and P. Piot, Beam dynamics simulations in a high-gradient X-band photoinjector, in *Proceedings of the 12th International Particle Accelerator Conference, IPAC-2021, Campinas, SP, Brazil* (JACoW, Geneva, Switzerland, 2021), WEPAB163, [10.18429/JACoW-IPAC2021-WEPAB163](https://doi.org/10.18429/JACoW-IPAC2021-WEPAB163).
- [24] W. Schottky, Über kalte und warme elektronenentladungen, *Z. Phys.* **14**, 63 (1923).
- [25] K. Flöttmann, Astra a space charge tracking algorithm, Version 3.2 (2017), available from DESY, Hamburg, Germany.
- [26] K.-J. Kim, rf and space-charge effects in laser-driven rf electron guns, *Nucl. Instrum. Methods Phys. Res., Sect. A* **275**, 201 (1989).
- [27] K. Flöttmann, rf-induced beam dynamics in rf guns and accelerating cavities, *Phys. Rev. ST Accel. Beams* **18**, 064801 (2015).